ORIGINAL PAPER



Transient Spark Discharge and Ozone-Driven Nitrogen Fixation to Water

Pankaj Pareek¹ · Gokul Selvaraj¹ · Karol Hensel¹ · Mário Janda¹

Received: 3 July 2025 / Accepted: 29 September 2025 © The Author(s) 2025

Abstract

Fixation of nitrogen and the generation of plasma-activated water are currently a significant focus within the low-temperature plasma research community. This study examines the enhancement of nitrogen fixation in water, by converting the weakly soluble nitrogen oxides (NO and NO₂) generated by transient spark (TS) to highly soluble dinitrogen pentoxide (N₂O₅) and nitric acid (HNO₃) in the gas phase. This is achieved by mixing ozone (O_3) with air that has been treated by a TS discharge. Without O_3 , only nitrite ions (NO_2^-) are detected in the water, formed primarily due to reaction between solvated NO and NO2. With addition of O₃ (400 ppm), the composition of species in water significantly changes depending on the initial NO/O₃ ratio. An excess of O₃ enables formation of N₂O₅ and HNO₃ in the gas and a high concentration of nitrate ions (NO₃⁻) in the water. With an excess of NO, the dominant gas phase product is NO₂ and a mixture of NO₂⁻ and NO₃⁻ is formed in the water by reaction between solvated NO2 molecules. Despite the additional energy required for O₃ generation, the overall energy efficiency for the formation of NOx (NO₂⁻+NO₃⁻) in the water increases fourfold, when enough N₂O₅ is formed. Further improvements are possible by optimizing the use of O₃ and ensuring all N₂O₅ is captured from the gas phase.

Keywords Nitrogen fixation \cdot Transient spark \cdot Ozone \cdot In-situ UV/Vis absorption spectroscopy

Published online: 14 October 2025

Faculty of Mathematics, Physics, and Informatics, Comenius University, Bratislava, Slovakia



Pankaj Pareek pareek1@uniba.sk

Mário Janda janda1@uniba.sk

Introduction

Plasma-induced chemistry is a highly complex process [1]. In dry air, non-equilibrium cold plasmas can generate various reactive oxygen and nitrogen species (RONS), such as O, N, N₂*, N₂O, NO, NO₂, N₂O₅, NO₃, and O₃ [2]. When water vapor is present, atmospheric plasma can also generate RONS like OH, H₂O₂, HNO₃, and HNO₂ [3–5].

The concentrations of individual RONS depend on the plasma source and input power. For example, Trunec et al. [6] investigated a coplanar dielectric barrier discharge in air and N_2/O_2 mixtures, finding that varying the input power (100–400 W) altered the gas-phase chemistry. At lower power, O_3 was the dominant species, while increasing the power led to a shift toward NO and NO_2 dominance. The density of N_2O_3 initially rises with increasing input power, but then sharply declines at the same power where O_3 density also drops.

When plasma is in contact with a liquid, such as water, the reactive chemical species generated by the plasma in the gas phase can dissolve in the liquid, producing a chemically rich solution called plasma-activated water (PAW) or plasma-treated liquid [7]. PAW has been widely studied over the past decade because the active chemistry provided by the various RONS, especially long-lived species like H₂O₂(aq), NO₂⁻(aq), and NO₃⁻(aq), can be utilized for medical, agricultural, and food preservation applications [8–12]. Cold plasma in contact with water is also used in wastewater treatment for the degradation of organic dyes and antibiotics [13, 14].

The reactive species in PAW can be generated by different pathways depending on the system configuration and on plasma source parameters, such as discharge power, gas flow rate, and treatment time. For example, in plasma jets, H₂O₂(aq) can be formed by the solvation of H₂O₂ formed in the gas phase by two-body recombination of OH radicals produced in the plasma [15, 16]. In pulsed discharges, H₂O₂(aq) in the PAW is mainly generated in the water by two-body recombination of dissolved OH(aq) radicals [17, 18].

The solubility of different gaseous RONS, typically described by Henry's law coefficient, is another factor influencing the production pathways of aqueous RONS [19, 20]. $NO_2^-(aq)$ can be formed by the reaction of solvated NO(aq) and $NO_2(aq)$ species [21]. However, in the presence of more soluble HNO_2 in the gas phase, its solvation becomes the dominant source of $NO_2^-(aq)$ [5]. Similarly, aqueous $NO_3^-(aq)$ can be formed by solvation of NO_2 , but much more efficient $NO_3^-(aq)$ formation in PAW can be obtained by solvation of more soluble N_2O_5 [22].

Furthermore, the rate of solvation of reactive species also depends on the size of the plasma/water interface. Transforming water into nebulized microdroplets with a large surface-to-volume ratio is preferable for the solvation of weakly soluble O₃, while highly soluble H₂O₂ is easily dissolved even in bulk water with a much smaller surface area compared to the surface of microdroplets with the same volume [19]. The charge of the microdroplets may also play a role. The formation of NO₂⁻(aq) from reactive nitrogen species (RNS) in charged electrospray microdroplets is more efficient than in neutral nebulized microdroplets [20].

The formation of plasma-activated water is therefore a very complex process, not fully understood. Basic research in this area is greatly needed, as there are still relatively few works that sufficiently address the composition of both gaseous and liquid species formed during PAW generation [23]. Additional research is therefore important for a better understanding of the formation mechanisms of reactive species in PAW and for assessing the role



of different gas-phase species in the formation of aqueous RONS. From a practical point of view, this knowledge will allow us to upscale used plasma sources, increase energy efficiency and improve selectivity with respect to the desired species when generating PAW.

The formation of PAW rich in reactive nitrogen species (RNS) is important for nitrogen fixation as an alternative process to the Haber–Bosch synthesis. At lower pressure, the fixation of nitrogen from air by microwave plasma can be more energy-efficient than the Haber–Bosch process, but in atmospheric pressure plasmas, energy efficiency is one of the drawbacks of nitrogen fixation that needs to be overcome [24]. If we consider the production of RNS in both the gas and liquid phases, as suggested by Luo et al., the apparent energy efficiency of RNS production may improve [23]. However, if the major part of gaseous RNS consists of weakly soluble NO or NO₂, and only a small fraction of them dissolves in the PAW (with the majority being wasted), it is necessary to focus on the generation of more soluble RNS, such as HNO₂ or N₂O₅, for a real increase in nitrogen fixation energy efficiency.

In transient spark (TS) discharges operated in dry air, the two dominant gaseous products are NO and NO₂. Even when operating in humid air, only a small portion of them is converted to HNO₂. Despite a significant increase in the NO₂⁻(aq) concentration in PAW generated by TS thanks to the formation of HNO₂ [5], the majority of gaseous RNS (NO and NO₂) do not readily dissolve in water. As an alternative, it is therefore necessary to consider the conversion of NO and NO₂ generated by TS to N₂O₅ through reactions with O₃ molecules [22].

Several studies have investigated the oxidation of NO by O_3 and the generation of N_2O_5 . Jõgi et al. showed that TiO_2 catalyst improved the oxidation efficiency of NO to N_2O_5 at $100~^{\circ}$ C [25]. Noori et al. utilized a dielectric barrier discharge (DBD) in O_2 gas to generate O_3 and introduced NO from a pressure tank to produce N_2O_5 , further studying the dissolution of RNS in water [26]. Wang et al. employed a gliding arc discharge to produce nitrogen oxides, while O_3 was generated using a DBD discharge to form N_2O_5 after mixing the output gases from these two plasma sources [22, 27]. They also hypothesized the importance of NO_3 for the formation of NO_3^- (aq) in the water exposed to the resulting gas mixture containing N_2O_5 and NO_3 [22]. Kaneko et al. developed a composite air plasma device capable of selectively generating high-density N_2O_5 for biomedical applications, including pathogen inactivation and amino acid modification [28].

This work investigates the potential to enhance nitrogen fixation by converting NO and NO₂ (NO_x) generated by TS discharges into N₂O₅ using O₃. We focus on the reaction mechanism at varying NO/O₃ ratios. Experimentally measured changes in gas composition are compared to theoretical results from a chemical kinetic model. After mixing NO_x and O₃, their resulting gas mixture passes through a water-filled cuvette, where NO₂⁻(aq) and NO₃⁻(aq) formation are measured in situ. Correlating gas-phase RNS, NO, NO₂, HNO₂, HNO₃, and N₂O₅, with NO₂⁻(aq) and NO₃⁻(aq), along with kinetic modeling, improves our understanding of nitrogen fixation in spark-like discharges. This knowledge can contribute to increasing the energy efficiency and upscaling of plasma-activated water production systems.



Experimental Setup

Figure 1 shows a simplified schematic of the experimental setup, which comprises several components. The plasma reactor (see details in Sect. "Plasma reactor and discharge diagnostics") generates NO and NO₂ using TS discharge. Dry synthetic air (80% N₂, 20% O₂, 99.99% purity), controlled at 0.8 L/min by a mass flow controller (Bronkhorst Flexi-Flow compact, flow controller 1 in Fig. 1), serves as the inlet gas.

At the plasma reactor outlet, the nitrogen oxide-containing gas is mixed with ozone-enriched air (0.2 L/min). Ozone is generated by a commercial ozone generator (Beyok FM-C300). Another mass flow controller (Bronkhorst Flexi-Flow compact, flow controller 2 in Fig. 1) controlled dry synthetic air at 1.5 L/min to the ozone generator inlet. The ozone generator outlet is connected to another flow controller (Aalborg P model rotameter, flow controller 3 in Fig. 1), allowing 0.2 L/min of ozone-enriched air to be mixed with the plasma-treated gas, so that O_3 concentration right after the mixing is 400 ± 30 ppm. The remaining ozone is exhausted. The NO and NO_2 concentrations in TS treated air varies with discharge power. The gas composition is measured by an FT-IR absorption spectrometer (see details in Sect. "FTIR absorption spectroscopy for diagnostics of gases").

The resulting gas mixture passes through a 2.5 m long Teflon tube (6 mm inner diameter). With a total gas flow rate of 1 L/min, the gas residence time in this tube is approximately 4.2 s. During this time, reactions between ozone and nitrogen oxides occur. Afterwards, the gas mixture either goes to the FTIR spectrometer or towards an enclosed quartz cuvette containing 3 mL of deionized (DI) water (initial conductivity $< 3 \mu S/cm$). In the cuvette, solva-

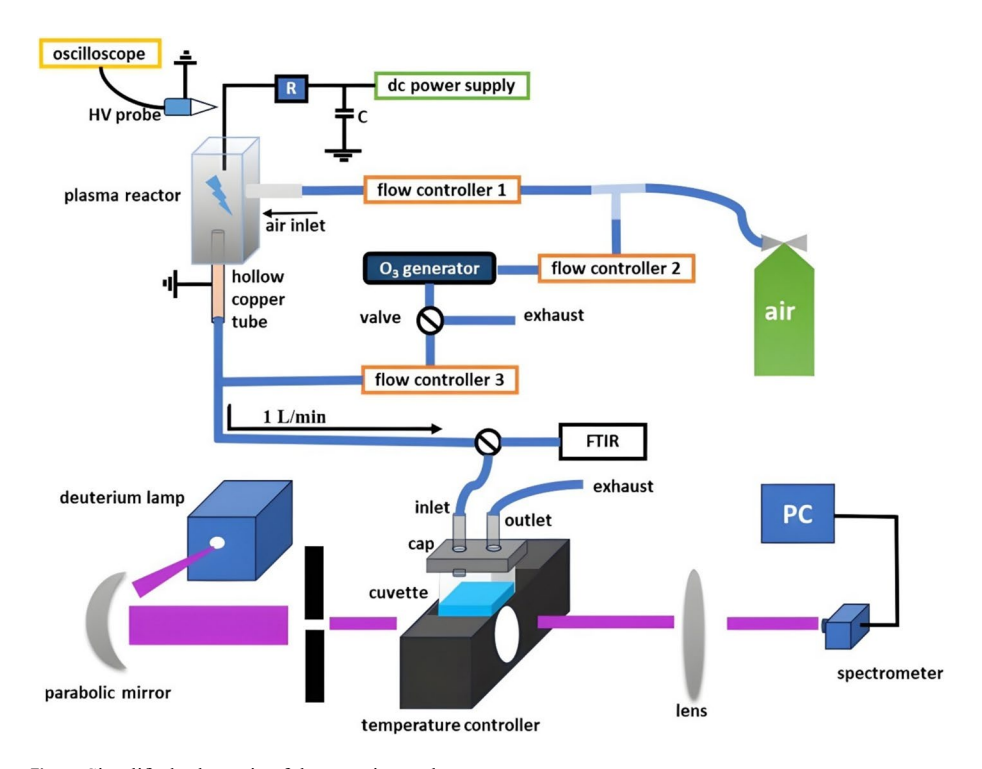


Fig. 1 Simplified schematic of the experimental setup



tion of gaseous RONS leads to a gradual increase in NO₂⁻(aq) and NO₃⁻(aq) concentrations in the water. These concentrations are monitored *in-situ* by UV/Vis absorption spectroscopy (see details in Sect. "In-situ UV/Vis absorption spectroscopy for diagnostics of liquids"). The water is exposed to the gas mixture for 1 or 3 min and then a change of pH and conductivity is measured by portable pH meter (WTW ProfiLine pH 3110) and conductivity meter (Greisinger GMH 3430), respectively.

For comparison, experiments are also performed without mixing nitrogen oxides with ozone, using either only plasma treated gas mixture with nitrogen oxides, or only 400 ppm of O_3 in the air. For all these experiments, a total air flow rate of 1 L/min is maintained. In experiments without O_3 , the air treated by TS (0.8 L/min) is mixed with dry synthetic air (0.2 L/min).

Plasma Reactor and Discharge Diagnostics

The reactor's high-voltage (HV) electrode is a sharpened M2 steel screw, and the ground electrode is a hollow copper tube (6 mm outer diameter, 5 mm inner diameter). The electrodes are housed within a Teflon block, separated by a gap of 8 ± 0.5 mm. Input gas enters the reactor through a 6 mm side inlet positioned near the tip of the HV electrode. The inner volume of the block is approximately $0.4 \, \mathrm{cm}^3$. After treatment, the plasma gas exits through the hollow copper ground electrode.

A transient spark (TS) discharge is generated between the HV electrode (anode) and the ground electrode using a high-voltage DC power supply (Spellman SL30P300). The electrical circuit includes an external resistor (4.6 M Ω) and an external capacitor (50 pF). The electrical properties of the TS discharge are assessed using a high-voltage (HV) probe (Cal Test Electronics CT4028) and a current monitor (Pearson Electronics 2877). The data are then analyzed with a digital oscilloscope (Tektronix TBS2104). Current and voltage waveforms are used to calculate the discharge power. The measurement of TS discharge power and input energy density was described in details in our previous publication [18].

FTIR Absorption Spectroscopy for Diagnostics of Gases

The main analytical technique used to determine the composition of the gas after treatment is IR absorption spectroscopy, using a gas cell with an optical path length of 10 cm equipped with CaF₂ windows. A Fourier transform infrared (FT-IR) spectrophotometer (Shimadzu IRSpirit) is used in a spectral range of 4000–1000 cm⁻¹ and a nominal spectral resolution of 0.9 cm⁻¹.

Since the FT-IR absorption technique is absolute, the concentration of RONS in the gas are obtained by fitting the measured spectra with a spectra calculated by our own script based on absorption lines for NO, NO_2 , HNO_3 , and O_3 downloaded from HITRAN database [29]. These absorption lines were convoluted with a Gaussian function to generate spectra that matched the spectral resolution of our spectrophotometer. We verified the calculated spectra against various concentrations NO and NO_2 prepared from calibrated gas mixtures of 2000 ppm NO in N_2 and 1000 ppm NO_2 in dry synthetic air (80% N_2 and 20% O_2). As there is no suitable set of absorption lines for N_2O_5 and HNO_2 , we are using absorption cross sections downloaded from the HITRAN database (for N_2O_5) and supplemental HITRAN database (for HNO_2) [30].



In-Situ UV/Vis Absorption Spectroscopy for Diagnostics of Liquids

In-situ UV/Vis absorption spectroscopy is employed for the detection of NO_2^- and NO_3^- produced in the liquid phase by the solvation of gaseous RNS. A quartz cuvette ($1 \times 1 \times 4$ cm) is placed inside a temperature controller (Shimadzu TCC-100), maintaining a temperature of 25 °C. The cuvette is filled with 3 mL of DI water (pH 5.9 and conductivity 2–3 μ S/cm). A deuterium lamp (Avantes AvaLight-D(H)-S) is used as a UV light source. A parallel light beam (approximately 3 mm in diameter) is formed using a parabolic mirror and an iris diaphragm, and it passes through the quartz cuvette 1 cm below the water surface. Absorbance spectra and the time evolution of reactive species are monitored using an microspectrometer (Ocean Insight ST-UV) with 2.2 nm resolution and 25 μ m slit.

Figures 2a and 2b show the absorption spectra of NO₂⁻(aq) and NO₃⁻(aq) standard solutions, prepared by dissolving accurate amounts of NaNO₂ and NaNO₃ in DI water. The NO₂⁻ (aq) spectra peak around 209–212 nm, and the NO₃⁻(aq) spectra peak around 203–205 nm are consistent with a literature [31, 32].

Quantitative analysis using absorption spectroscopy is based on the Beer-Lambert law, expressed as $A = \varepsilon(\lambda)cL$, where A represents absorbance, ε is the molar extinction coefficient (or absorptivity) changing with the wavelength λ , L is the absorption path length, and c is the concentration of the absorbing species. When the same optical cell is used (i.e., L is constant) for both standard and unknown samples, the equation simplifies to $A = k(\lambda)c$, where $k(\lambda)$ is the proportionality function.

For multicomponent systems, where multiple absorbing species are present, the total absorbance is the sum of the individual absorbances of each component. This requires considering the contribution of each species to the overall spectrum. Multicomponent spectroscopic analysis, as described by Brown et al.[33], provides a framework for this. In this context, the Beer-Lambert law can be expressed in a matrix form, A = KC, or as:

$$\begin{bmatrix} A_{1}' & A_{1}'' & \dots & A_{1}^{m} \\ A_{2}' & A_{2}'' & \dots & A_{2}^{m} \\ \dots & \dots & \dots & \dots \\ A_{i}' & A_{i}'' & \dots & A_{i}^{m} \end{bmatrix} = \begin{bmatrix} k_{11} & k_{12} & \dots & k_{1n} \\ k_{21} & k_{22} & \dots & k_{2n} \\ \dots & \dots & \dots & \dots \\ \vdots & \dots & \dots & \dots \\ k_{i1} & k_{i2} & \dots & k_{in} \end{bmatrix} \begin{bmatrix} c_{1}' & c_{1}'' & \dots & c_{1}^{m} \\ c_{2}' & c_{2}'' & \dots & c_{2}^{m} \\ \dots & \dots & \dots & \dots \\ \vdots & \dots & \dots & \dots \\ c_{n}' & c_{n}'' & \dots & c_{n}^{m} \end{bmatrix}$$
(1)

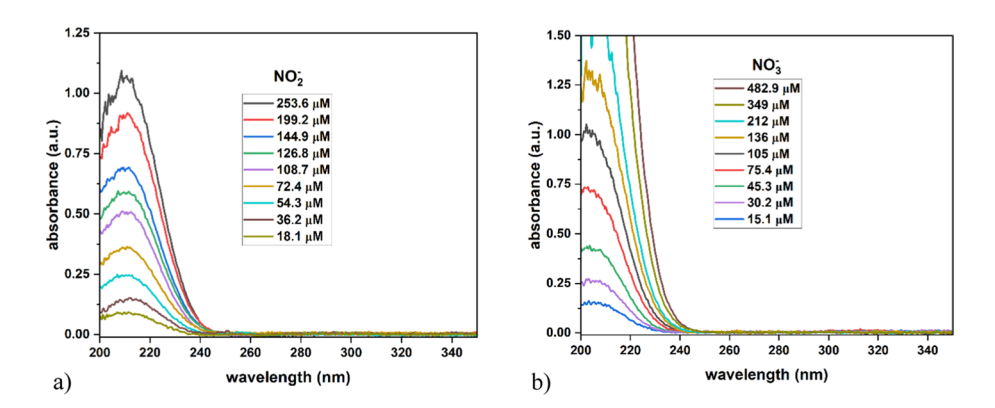


Fig. 2 Absorption spectra of $NO_2^-(\mathbf{a})$, and $NO_3^-(\mathbf{b})$ standard solutions



The absorbance matrix **A** $(i \times m)$ contains the absorbance values of m standard solutions at i wavelengths. The concentration matrix **C** $(n \times m)$ holds the concentrations of n components in each standard solution, with $i \ge n$.

To determine the concentrations of components in an unknown mixture, the molar absorptivity matrix \mathbf{K} must first be calculated. This matrix can be derived using the equation:

$$\mathbf{K} = \mathbf{AC}^T (\mathbf{CC}^T)^{-1} \tag{2}$$

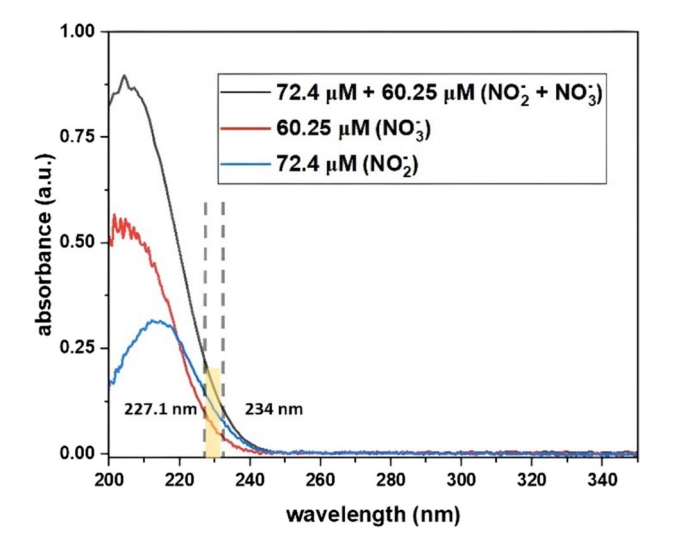
where C^T represents the transpose of the concentration matrix C. Once the K matrix is known, the concentrations of the components in an unknown mixture can be calculated using the formula.

$$\mathbf{C} = \left(\mathbf{K}^T \mathbf{K}\right)^{-1} \mathbf{K}^T \mathbf{A} \tag{3}$$

He et al. employed multicomponent analysis using the first derivative method to simultaneously detect $H_2O_2(aq)$, $NO_2^-(aq)$, and $NO_3^-(aq)$ [34]. In our study, hydrogen peroxide was excluded from the calibration due to its absence, as demonstrated in our previous work [18]. For this analysis, we utilized n=2 components (NO_2^- and NO_3^-), m=24 standard solutions, and i=21 absorbance data points. Absorbance data within the wavelength range of 227.1 nm to 233.9 nm were used (Fig. 3). This specific range was chosen because at lower wavelengths, the absorbance of NO_3^- (aq) becomes excessively strong, and spectra below 210 nm are susceptible to pH influence, as previously described by Liu et al. [31].

Following the determination of the **K** matrix, its reliability was assessed by quantifying the concentrations of NO_2 ⁻(aq) and NO_3 ⁻(aq) in a series of blind samples. The relative differences between the measured and known concentrations were found to be 2.1–6.4% for NO_2 ⁻(aq) and 0.4–3.4% for NO_3 ⁻(aq). The step-by-step process for the determination of $(\mathbf{K}^T\mathbf{K})^{-1}\mathbf{K}^T$ matrix is shown in Supplementary material I. The measured concentrations of NO_2 ⁻(aq) and NO_3 ⁻(aq) were subsequently used to calculate the overall energy efficiency (η [mol.J⁻¹]) using the formula:

Fig. 3 Illustrative absorption spectra of NO₂-(aq), NO₃-(aq), and their mixture, showing wavelength range (~ 227–234 nm) from which K matrix coefficients were calculated





$$\eta = \frac{\left[NO_x^-\right].V}{P_d.\Delta t} \tag{4}$$

Here, $[NO_x^-]$ represents the sum of the concentrations of NO_2^- (aq) and NO_3^- (aq) in the water, V is the volume of the water, P_d is the discharge power, and Δt is the treatment time. In case of experiments with O_3 , we added 8 W to P_d , to take into account the power used by ozone generator.

Chemical Kinetic Modeling

Chemical kinetic modeling is a powerful computational tool used to understand and predict how the density of different chemical species change over time in complex systems, including their gas phase production and loss pathways [35]. It is useful when experiments or analytical calculations are not capable to measure or predict concentrations of some important species in studied system.

Temporal evolution of density N_i of all species X_i in a kinetic model can be derived from the used reaction set as

$$\frac{\mathrm{d}N_i}{\mathrm{d}t} = \sum_{j=1}^{j=n} \left(a - a'\right) \times R_j \tag{5}$$

Here, R_j is a rate of the j^{th} chemical reaction, a and a' are stoichiometric coefficients of the X_i species in the j^{th} reaction.

$$aX_i + bX_{i+1} + \dots \to a'X_i + b'X_i + l + \dots$$
 (6)

The reaction rate R_i can be expressed as.

$$R_j = k_j \times \prod_{m=i}^{m=i+l} N_m^{\alpha_m} \tag{7}$$

where k_j is the reaction rate coefficient, l is the total number of species involved in the j^{th} reaction, N_m is the actual density of the m^{th} species, and α_m is the partial order of the reaction j^{th} with respect to the species m.

Solving this set of reactions numerically is typically required, necessitating the use of a differential equation solver. Our model leverages the ZDPlasKin module [36], which incorporates a Fortran 90 implementation of the VODE solver [37]. VODE utilizes Adams' or backward differentiation formula methods for solving systems of ordinary differential equations. Furthermore, we utilize the comprehensive list of chemical processes and rate coefficients for nitrogen—oxygen mixtures provided by the ZDPlasKin authors [38], which is based on reactions documented in [39] and [40] (see Supplementary material II).

The rate coefficients for reactions between heavy species are calculated using the thermodynamic gas temperature $T_{\rm g}$. In contrast, the rate constants for electron impact reactions require the electron energy distribution function (EEDF). The EEDF is determined by solving the Boltzmann equation for free electrons. While the ZDPlasKin package includes the



Bolsig +solver [41] for this purpose, we did not utilize this feature in our model. Since our focus was on reactions occurring among gas-phase species after exiting the plasma reactor, we assumed a constant electron density of 10³ cm⁻³. At this low electron density, the influence of electrons on the ongoing chemistry is negligible.

Results and Discussion

This chapter begins with a discussion of the electrical characteristics of the TS discharge and the resulting gas-phase chemistry in dry synthetic air (Sect. "TS discharge in dry synthetic air"). Subsequently, we explore the correlation between the gas composition and the composition of RNS in water exposed to plasma-treated air (Sect. "Properties of water exposed to dry air treated by TS"). Furthermore, we present the changes in the plasma-treated air composition following its mixing with ozone-enriched air. These experimental data are then compared with computational results (Sect. "Gas phase chemistry in mixtures with NO, NO2 and O3"). Finally, we present the changes in water composition due to the presence of ozone (Sect. "Properties of water exposed to dry air treated by TS, mixed with O3").

TS discharge in Dry Synthetic Air

Although a DC power supply is used, the transient spark discharge is a self-pulsing phenomenon due to the repetitive charging and discharging of the driving circuit capacitance C, with a typical repetition frequency f=1-10 kHz [42, 43]. During the charging phase of capacitance C, the voltage applied to the anode increases until it reaches the characteristic gas breakdown voltage. Gas breakdown then initiates a rapid discharge of the driving circuit capacitance, resulting in the formation of a short, high-current spark pulse, as shown in Figure S1 (Supplementary material III).

The frequency of the TS current pulses can be controlled by adjusting the mean current supplied to the circuit by the HV power generator, I_g . An increase in the generator mean current leads to faster charging of the circuit capacitance and a higher TS repetition frequency. It can be validated from Figure S2 (Supplementary material III), showing long scale waveforms at 0.6 mA and 1.5 mA. In the experiments presented in this paper, the TS repetition frequency was varied approximately within the range of 0.7–3 kHz by adjusting the average current supplied to the circuit by the HV power supply within the range of 0.6–1.5 mA. Figure 4 illustrates the discharge power, P_d , and the input energy density as functions of the mean current provided by the power supply. As I_g increases, both the input energy density and the power delivered to the gas by the transient spark discharge also increase. The input energy density is a crucial factor in evaluating the energy efficiency of chemical product formation via TS discharge. By regulating input energy density, the mean current thus indirectly also controls the concentration of nitrogen oxides generated by TS discharge.

Figure 5 illustrates the concentrations of NO, NO₂, and NOx (i.e. sum of NO and NO₂) as a function of increasing generator mean current. The NO concentration increases from 140 to 490 ppm, while the NO₂ concentration increases from 105 to 160 ppm, as the mean current rises from 0.6 mA to 1.5 mA. Higher NOx concentrations with improved energy efficiency can be achieved by modifying the reactor design and circuit parameters, such as by incorporating an additional inductance, as we reported recently [44]. However, the primary



Fig. 4 The discharge power, Pd, and the input energy density as functions of the mean current

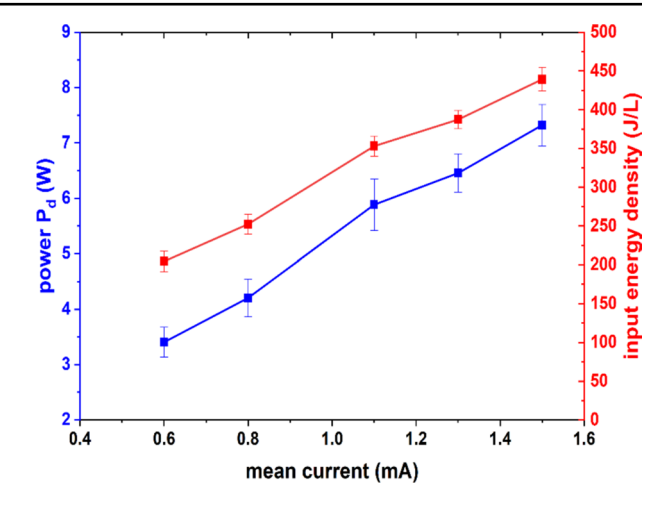
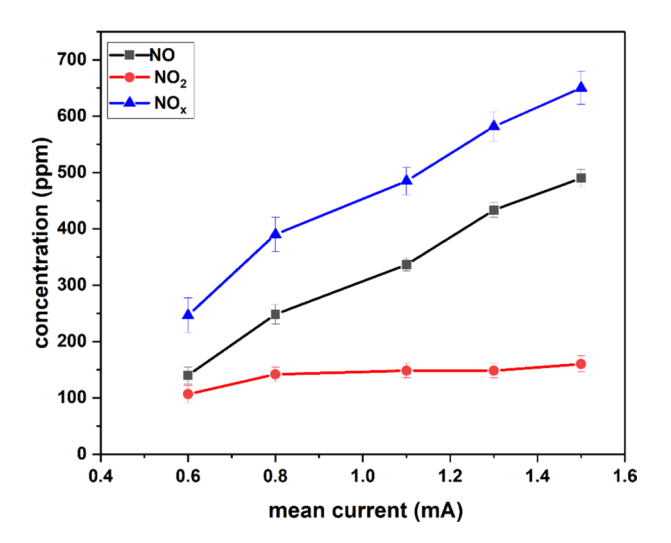


Fig. 5 The concentrations of NO, NO₂, and NOx as a function of mean current; measured after mixing 0.8 L/min of TS treated air with 0.2 L/min of dry synthetic air



objective of this paper is not the optimization of NOx generation in the gas phase, but rather the investigation of the correlation between gas and liquid phase chemistry, with the aim of enhancing the efficiency of aqueous RNS formation.

Properties of Water Exposed to Dry Air Treated by TS

Dry air treated by the TS discharge was passed over DI water in a cuvette for 3 min at a total gas flow rate of 1 L/min. The concentrations of NO_2 -(aq) and NO_3 -(aq) in the water, C_{NO2} - and C_{NO3} -, were continuously monitored by recording absorption spectra every 10 s. Figure 6a depicts the time evolution of NO_2 -(aq) concentration for various mean discharge currents. In all cases, the NO_2 -(aq) concentration increased linearly with time, within experimental uncertainty. Notably, NO_3 -(aq) was not detected in the water.



Figure 6b shows that the NO₂⁻(aq) concentration after 160 s increased as the mean current increased, which can be attributed to the corresponding increase in NOx concentration in the gas phase (Fig. 5). Figure 6b also shows the dependence of the pH after the treatment on the mean current. At a mean current of 1.5 mA, the pH decreased from 5.8 to 3.9. At lower mean currents, the pH after the treatment decreased less, reaching 4.1 at I_g =0.6 mA. In addition, the conductivity of the water increased from 2–3 μ S/cm up to approximately 30 μ S/cm at I_g =0.6 mA. With increasing mean current, the conductivity further increased to approximately 50 μ S/cm at I_e =1.5 mA.

Komiyam et al. demonstrated that in a gas mixture containing NO and NO₂, if the solvation of these species into water is diffusion-limited, the resulting water chemistry is primarily dominated by NO_2^- [45]. In our experiment, we assume that the solvation of NO and NO_2 is similarly diffusion-limited, supported by the low gas flow rate and absence of significant water surface agitation. Therefore, the reaction kinetics and the concentrations of NO_2^- (aq) and NO_3^- (aq) in the liquid depend on the uptake (flux) of gas-phase NOx into the water, and the build-up of NO(aq) and NO_2 (aq) concentrations. Subsequent aqueous reactions between these species can then lead to NO_2^- formation:

$$NO(aq) + NO_2(aq) + H_2O \rightarrow 2NO_2^-(aq) + 2H^+(k_8 = 1.6 \times 10^8 M^{-1} s^{-1}),$$
 (8)

$$2NO_2(aq) + H_2O \to NO_2^-(aq) + NO_3^-(aq) + 2H^+(k_9 = 8.4 \times 10^7 M^{-1} s^{-1}).$$
 (9)

At low pH, NO₂⁻ (aq) is subsequently converted to NO₃⁻ (aq) by a disproportionation reaction [19]

$$3NO_2^-(aq) + 3H^+ \to 2NO(aq)^+ + NO_3^-(aq) + H_3O^+.$$
 (10)

However, even at pH 3.4, the decrease of NO₂⁻ (aq) concentration is relatively slow, with characteristic times exceeding 2000 min [18]. In our experiment, the treatment time is only 3 min and the pH did not fall below 3.9. Relatively low decrease of pH can be also attributed to the low concentration of NO₃⁻ ions in the water. To understand why NO₃⁻ was not detected, let's examine reactions (8) and (9).

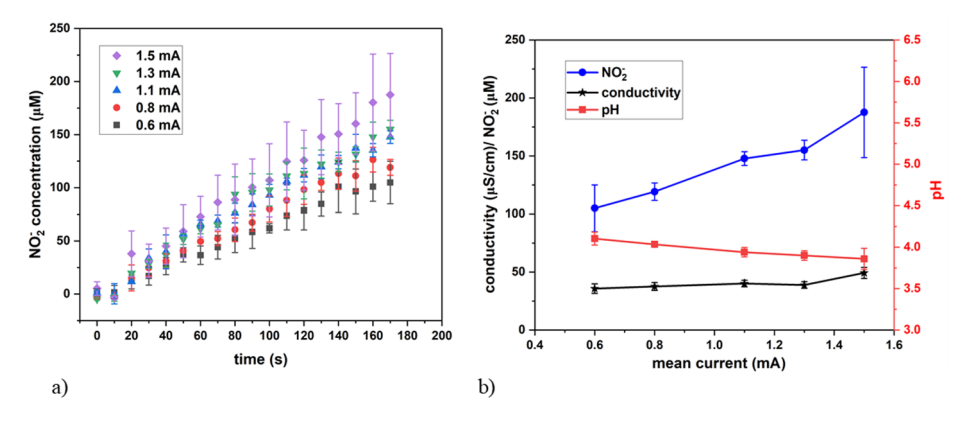


Fig. 6 Time evolution of NO₂⁻(aq) concentration in water (a), and dependence of the final NO₂⁻(aq) concentration, pH and conductivity on mean current (b)

Production of NO₂⁻(aq) and NO₃⁻(aq) depends on rate coefficients of reactions (8) and (9), and concentration of reactants, NO(aq) and NO₂(aq). We do not know exact concentrations of NO(aq) and NO₂(aq) in the treated water, but we derived an approximate formula describing dependence of C_{NO2} - $/C_{NO3}$ - on ratio of NO(aq) to NO₂(aq) concentrations, C_{NOaq} / C_{NO2aq} (see Supplement IV for details):

$$C_{NO2-}/C_{NO3-} \approx 4C_{NOaq}/C_{NO2aq} + 1.$$
 (11)

According to Henry's law, the aqueous phase concentration of species under steady-state conditions is proportional to its partial pressure in the gas phase. Henry's law solubility coefficient of NO_2 is roughly six times higher than solubility coefficient of NO [46]. Given that gas-phase NO concentration is three times higher than NO_2 (490 ppm vs. 160 ppm at I_g =1.5 mA, Fig. 5), Henry's law predicts a steady-state NO_2 (aq) concentration twice that of NO(aq). Based on Eq. (11), if C_{NO2aq}/C_{NO2aq} =0.5, it would result in a NO_2 -(aq) to NO_3 -(aq) concentration ratio of 3:1, predicting a final NO_3 -(aq) concentration of approximately 60 μ M when C_{NO2} - reaches 180 μ M.

The lack of NO_3^- (aq) observed experimentally thus suggests that our system is not at steady-state due to the short experiment duration and continuous consumption of NO(aq) and $NO_2(aq)$ by reactions (8) and (9). Therefore, NO(aq) and $NO_2(aq)$ concentrations are not determined by Henry's law solubility coefficients. We assume that they are rather directly proportional to gas-phase NO(aq) and $NO_2(aq)$, based on gas-phase NO(aq) concentrations is potentially three times higher than $NO_2(aq)$, based on gas-phase NO/NO_2 ratio, the C_{NO2} to C_{NO3} ratio becomes 13:1, according to Eq. (11), predicting only ~14 μ M concentration of NO_3^- (aq), when NO_2^- (aq) concentration is 180 μ M. While 15 μ M concentration of NO_3^- (aq) is detectable in pure NO_3^- (aq) solution (Fig. 2b), it approaches the detection limit in the presence of significantly higher NO_2^- (aq) concentrations (~180 μ M).

Additionally, other $NO_2^-(aq)$ production pathways may further increase the C_{NO2}^- to C_{NO3}^- ratio. For example, N_2O_3 can form in a NO and NO_2 gas mixture as an intermediate product in the gas phase or at the liquid interface, resulting in $NO_2^-(aq)$ formation in water via reaction (12) [45, 47, 48]:

$$N_2O_3 + H_2O \to 2NO_2^-(aq) + 2H^+.$$
 (12)

Gas Phase Chemistry in Mixtures with NO, NO₂and O₃

Introducing O₃ into the TS discharge-treated gas stream, containing NO and NO₂, generated additional species identified by FT-IR spectroscopy. At input mean currents of 0.6, 0.8, and 1.1 mA, the FT-IR spectra showed N₂O₅, HNO₃, and NO₂ absorption bands. At 1.3 and 1.5 mA, N₂O₅ concentration was minimal (around 3 ppm), and NO₂ concentration was significantly high (above 500 ppm) and some NO was also detected (up to 150 ppm at 1.5 mA). Figure 7a presents illustrative FT-IR spectra, demonstrating significant variations in the resulting gas mixture composition approximately 4 s after mixing O₃ (initial concentration 400 ppm) with TS-treated air at different mean currents and different initial NOx concentrations (Fig. 5).



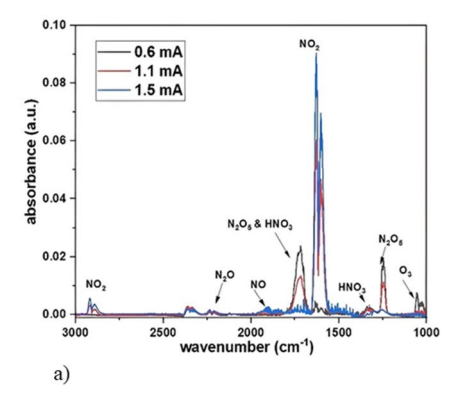
The influence of NO and NO_2 generated by the ozone generator on overall NOx concentrations was found to be negligible. The TS generated much higher concentrations of NO and NO_2 than the ozone generator, and the TS-treated air was mixed with O_3 -rich air from the ozone generator in a 4:1 ratio. Only N_2O was generated more efficiently by the ozone generator than by the TS discharge. However, as also shown by our kinetic modeling, N_2O is a very stable molecule and can be considered inert in the post-plasma chemistry.

Figure 7b provides a zoomed-in view of one spectrum (wavenumbers $1400-1000 \text{ cm}^{-1}$, $I_g=0.6 \text{ mA}$), illustrating the fitting procedure used to calculate individual product concentrations.

Figure 8 shows the relationship between mean current and measured O₃, NO, NO₂, and N₂O₅ concentrations. A notable shift in product distribution occurs around a mean current of 1.2 mA. At low mean current (below 1.2 mA), N₂O₅ concentration is high, peaking around 110 ppm at 0.8 mA, while NO is fully consumed. O₃ concentration decreases and is completely consumed above 1.2 mA. NO₂ concentration increases from 0.6 to 1.5 mA, reaching approximately 580 ppm at high mean current.

Measured data are compared with chemical kinetic model values. The model used an initial O_3 concentration of 400 ppm, and NO and NO₂ concentrations from Fig. 5. Chemical composition changes were tracked for 4 s in the model. The calculation step varied from 0.1 ns to 10 μ s and was adjusted after each step to ensure relative changes of species concentration did not exceed 10%. It is evident that, for all species considered, the experimental and computationally derived concentrations demonstrate a consistent dependence on the mean current. Furthermore, the corresponding experimental and computational data points presented in Fig. 8 display close agreement. Notably, the majority of computational points are situated within the experimental uncertainty range of the measured data points. Consequently, we can confidently utilize the model to approximate the concentrations of species that are not experimentally observable (e.g. NO₃), however infer the reaction pathways involved in N₂O₅ formation.

Figure 9 illustrates the computationally derived time evolution of NO, NO₂, O₃, and N₂O₅ species under two limiting conditions. Figure 9a presents data simulating I_g =0.6 mA, characterized by the lowest initial concentrations of NO and NO₂, specifically 145 ppm and



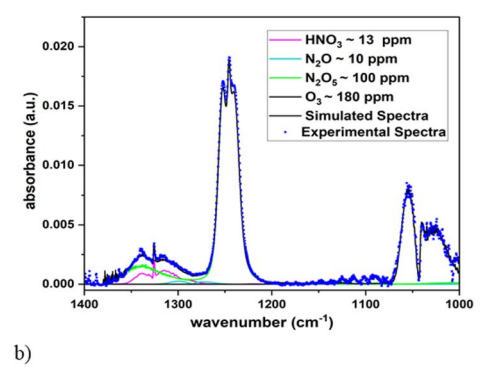
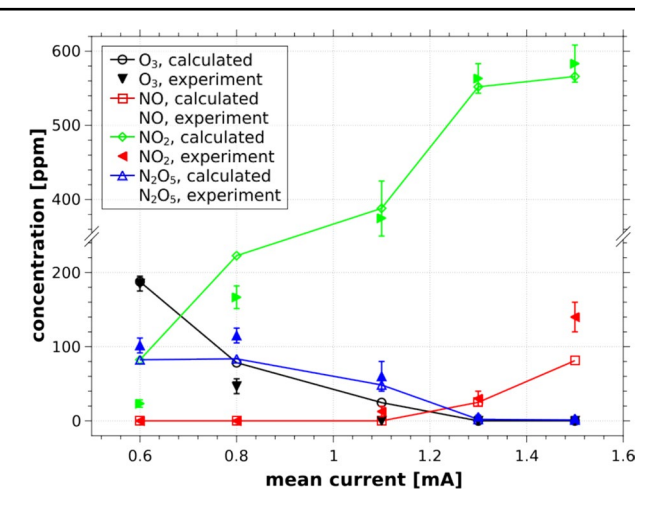


Fig. 7 FT-IR spectra of gas mixture approximately 4 seconds after mixing O_3 (initial concentration 400 ppm) with TS-treated air at different mean currents (a); zoomed-in view of a spectrum, wavenumbers $1400-1000 \text{ cm}^{-1}$, Ig = 0.6 mA (b)

Fig. 8 The dependence of measured O₃, NO, NO₂, and N₂O₅ concentrations (experiment) on a mean current; comparison with chemical kinetic model values (calculated)



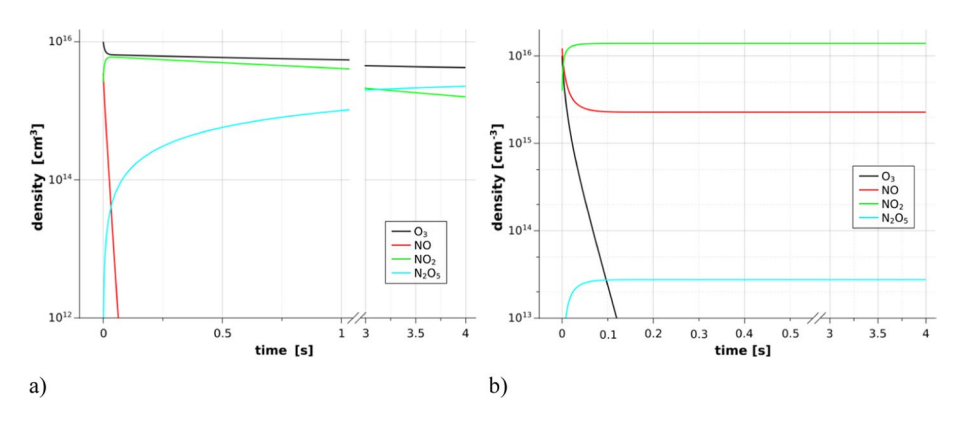


Fig. 9 Computationally derived time evolution of NO, NO₂, O₃, and N₂O₅ species under two limiting conditions; (a) data simulating I_g =0.6 mA; (b) data simulating I_g =1.5 mA

100 ppm, respectively. Figure 9b presents data simulating I_g =1.5 mA, characterized by the highest initial concentrations of NO and NO₂, namely 490 ppm and 145 ppm, respectively.

Figure 9a demonstrates that NO is consumed relatively quickly, within less than 0.1 s, together with a noticeable reduction in O₃ concentration and an increase in NO₂ concentration. This phenomenon is attributed to the mutual reaction between NO and O₃ species, yielding NO₂:

$$NO + O_3 \rightarrow NO_2 + O_2 \tag{13}$$

Given that at 0.6 mA the initial concentration of O₃ significantly surpasses that of NO, the remaining ozone proceeds to react with NO₂, oxidizing it to the nitrate radical (NO₃):

$$NO_2 + O_3 \to NO_3 + O_2$$
 (14)



Reaction (14) exhibits a considerably slower rate compared to reaction (13) and progresses gradually throughout the entire simulation period. However, NO₃ does not accumulate in the gaseous phase, its number density remaining below 10¹⁰ cm⁻³ (hence, it is not depicted in Fig. 9), as it is consumed by its reaction with NO₂, resulting in the formation of N₂O₅:

$$NO_2 + NO_3 + M \to N_2O_5 + M$$
 (15)

This observation suggests that reaction (13) is the limiting factor for the production of N_2O_5 . The gradual increase in N_2O_5 concentration observed throughout the computational time aligns with the findings of Wang et al., who demonstrated that the concentration of N_2O_5 is dependent upon the tube length, which corresponds to the interaction time between O_3 and NOx [27]. In general, our results are consistent with prior research that has investigated the production of N_2O_5 [26, 27]. Furthermore, the observed results align with established night atmospheric chemistry, in which the NO_3 radical plays a crucial role as an oxidation agent [49]. It is important to note, however, that the initial concentrations of NO, NO_2 , and O_3 in the studied gas mixture were significantly higher than those in the atmosphere.

The situation depicted in Fig. 9b, corresponding to 1.5 mA, presents a distinct scenario. Given that at 1.5 mA the initial concentration of O₃ is lower than that of NO, the mutual reaction (13) between these species results in the complete depletion of O₃ within less than 0.2 s, causing a significant elevation in the concentration of NO₂. Subsequent oxidation to NO₃ is impossible, and consequently, the concentration of N₂O₅ remains at a low level, plateauing around the 0.1-s mark. For the remainder of the simulation period, the concentrations of NO and NO₂ exhibit minimal variations, too.

Despite using dry synthetic air, HNO₃ was observed in FT-IR spectra at discharge currents below 1.2 mA, reaching concentrations up to approximately 20 ppm. We hypothesize that this HNO₃ formation resulted from the hydrolysis of N₂O₅ by trace water molecules, a process analogous to nighttime atmospheric chemistry [50, 51]. Potential sources of this water include residual moisture in the synthetic air, water absorbed on tubing surfaces, and diffusion from the silica tubes connecting the Teflon components to the reactor and FT-IR cell. However, our kinetic model does not account for humidity, because atmospheric HNO₃ production via N₂O₅ hydrolysis primarily occurs through heterogeneous surface reactions on water aerosol particles [52], not solely gas-phase mechanisms. Therefore, a more comprehensive model incorporating both gas-phase and surface reactions, along with a precise characterization of reactive surface sites within our system, and formation of aerosol would be necessary to model HNO₃ formation.

Properties of Water Exposed to Dry Air Treated by TS, Mixed with O₃

Figure 10a presents the time-dependent concentrations of NO₂⁻(aq) and NO₃⁻(aq) in water subjected to dry air treated by a TS discharge and subsequently mixed with O₃. Data are shown for different mean currents. Figure 10b displays the trends of pH, conductivity, and the final NO₂⁻(aq) and NO₃⁻(aq) concentration after a 65 s treatment period, plotted against the mean current. In contrast to experiments without supplemental O₃, where the water was exposed to the reactive nitrogen species mixture for three minutes, here the water was exposed to RNS mixture for only one minute. This restriction was imposed because, at mean



currents below 1.2 mA, the NO₃⁻(aq) concentration increased too rapidly, surpassing the upper limit of the in-situ absorption spectroscopic technique.

A clear distinction in the data between low and high mean currents is observed in both figures, which is caused by variations in the initial NO to O_3 ratio and thus different composition of gas entering the cuvette. At mean currents exceeding 1.2 mA, where the initial NO concentration surpasses the O_3 concentration, NO_2 becomes the dominant gas species entering the cuvette (Fig. 8). Specifically, at I_g =1.3 mA, the formation of NO_2 -(aq) and NO_3 -(aq) occurs through reaction (9), involving two solvated NO_2 (aq) molecules. Consequently, the concentrations of NO_2 -(aq) and NO_3 -(aq) are nearly equal, within the experimental uncertainty (Fig. 10a).

At I_g =1.5 mA, the gas composition entering the cuvette is slightly altered; in addition to NO₂, some residual NO is present. This leads to a slightly higher concentration of NO₂⁻(aq) compared to NO₃⁻(aq). This difference arises because NO₃⁻(aq) is exclusively produced via reaction (9), whereas NO₂⁻(aq) is generated by both reaction (8) and reaction (9). At both 1.3 mA and 1.5 mA, the pH decreases below 4, similar to the pH observed in water exposed to TS treated air without supplemental O₃ (Fig. 6b).

The situation differs at mean currents below 1.2 mA, where the initial NO concentration is lower than the initial O_3 concentration. High NO_3 –(aq) concentration was observed, while the NO_2 –(aq) concentration was negligible. This discrepancy can be attributed to the presence of N_2O_5 and HNO_3 in the gas phase. HNO_3 is highly soluble and readily dissolves in the liquid, yielding nitrate:

$$HNO_3(g) \to HNO_3(aq) \to NO_3^-(aq) + H^+$$
 (16)

 N_2O_5 can generate NO_3^- (aq) in water through two pathways [22, 27]. First, gaseous N_2O_5 can dissolve directly into the liquid, producing NO_3^- (aq) via reaction (17):

$$N_2 O_5(aq) + H_2 O \to 2 NO_3^-(aq) + 2H^+$$
 (17)

Second, it can form HNO₃ at the liquid interface through reaction (18), subsequently dissolving according to reaction (16):

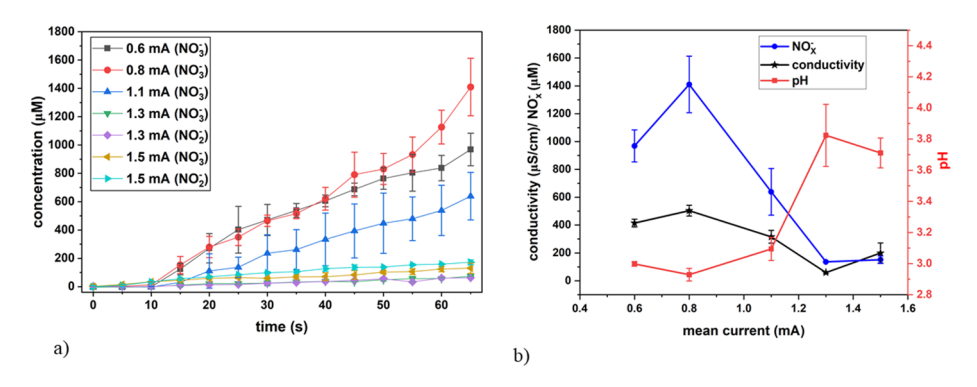
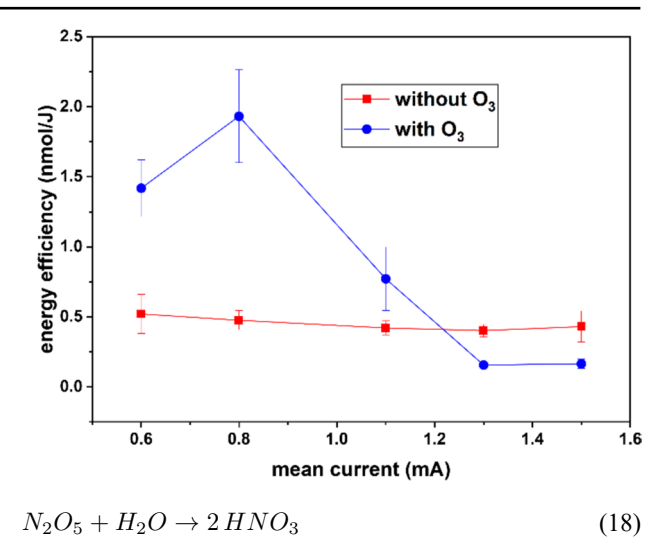


Fig. 10 Time evolution of $NO_2^-(aq)$ and $NO_3^-(aq)$ concentrations in water (a), and dependence of the final NO_x^- concentration, pH and conductivity on mean current (b)



Fig. 11 Energy efficiency of NO_x⁻ (aq) (NO₂⁻(aq)+ NO₃⁻ (aq)) formation from dry air treated by TS, with and without additional O₃, dependence on mean current



The sharp decrease in pH and high conductivity observed after one minute of treatment at I_{σ} < 1.2 mA are a direct consequence of the elevated H⁺(aq) and NO₃⁻(aq) concentrations.

Figure 11 shows the energy efficiency of NO_x^- formation from dry air treated by TS discharge, with and without additional O_3 , as a function of mean current. When calculating energy efficiency with additional O_3 , the power consumed by the ozone generator was included. Despite this, the highest efficiency achieved with O_3 is approximately 2 nmol/J, which is four times higher than that obtained using TS discharge alone. This calculation used the total ozone generator power (8 W), while only a fraction of the generated ozone was utilized. Therefore, efficiency could be further improved by utilizing different ozone source, generating less O_3 at lower power.

The efficiency of NO_x^- fixation peaks at 0.8 mA, coinciding with the maximum observed concentrations of N_2O_5 and HNO_3 . This suggests that N_2O_5/HNO_3 are key reactive species for nitrogen fixation in water. At 0.8 mA, the gas-phase concentrations of N_2O_5 and HNO_3 are approximately 115 ppm and 21 ppm, respectively. In the liquid phase, the NO_3^- concentration after one minute of treatment is approximately 87 ppm. If HNO_3 is assumed to dissolve completely, it accounts for about 24% of the total NO_3^- in the water. The remaining NO_3^- (aq), approximately 66 ppm, is attributed to the solvation of N_2O_5 .

Since one N_2O_5 molecule produces two $NO_3^-(aq)$ ions in the liquid phase via reaction (17), only roughly 29% of the gas-phase N_2O_5 dissolves into the liquid under the present experimental conditions. Noori et al. [26] reported its higher solvation efficiency of approximately 78%. This significant discrepancy could be due to the limited gas-liquid interaction area and diffusion-limited transport in our setup. The solvation efficiency of N_2O_5 can be further improved by bubbling the treated gas through the water or by using an electrospray system, which significantly increases the total interaction interface by converting bulk water into microdroplets [19].



Conclusions

This study investigates reaction pathways that enhance nitrogen fixation by combining air treated with transient spark discharge, containing NO and NO₂, with O₃ generated by an ozone generator. The resulting gas mixtures were passed through a cuvette filled with deionized water, where in-situ UV–Vis absorption spectroscopy was used to analyze the liquid-phase reactive nitrogen species. A key novelty of this work is the correlation between gas-phase and liquid-phase RNS concentrations. Gas-phase RNS, quantified by FT-IR absorption spectroscopy, were compared with values calculated by a chemical kinetic model. A good agreement between measured and calculated gas-phase RNS was achieved, validating the model's utility in elucidating the reaction mechanism for N₂O₅ production.

The TS discharge efficiently generates NO and NO₂ in dry air. In these experiments, the NO concentration ranged from 140 to 490 ppm, while the initial NO₂ concentration was always lower, ranging from 90 to 160 ppm. When only TS-treated air was passed through the cuvette (without additional O₃), NO₂⁻(aq) accumulation was observed, with negligible NO₃⁻ (aq) formation. This suggests that NO₂⁻(aq) formation is primarily driven by the reaction between solvated NO(aq) and NO₂(aq). However, due to the limited solubility of NO and NO₂, only a small fraction dissolved in the water.

Mixing TS-treated air with O_3 (initial concentration 400 ppm) significantly altered concentrations of RNS both in gas and liquid-phase. The NO to O_3 ratio was the critical factor determining the reaction pathway. Initially, NO reacts with O_3 to produce NO_2 . If the NO concentration exceeded the O_3 concentration, the dominant gas-phase products entering the water cuvette were NO_2 and residual NO. Consequently, the water contained a mixture of NO_2 -(aq) and NO_3 -(aq), primarily formed by the reaction of two solvated NO_2 (aq) molecules. On the contrary, if the O_3 concentration exceeded the NO concentration, NO was completely oxidized to NO_2 and further to NO_3 . This highly reactive radical rapidly reacts with NO_2 to produce N_2O_5 . The rate-limiting step for N_2O_5 formation is the relatively slow reaction between O_3 and NO_2 .

The kinetic model highlighted the crucial role of NO_3 in N_2O_5 formation. However, due to its low gas-phase concentration (resulting from its slow production and rapid consumption), direct NO_3 solvation contributed negligibly to aqueous RNS formation. Instead, NO_3 indirectly influenced aqueous RNS production through the formation of highly soluble N_2O_5 .

 N_2O_5 solvation leads to the direct formation of NO_3^- (aq) or indirect formation via HNO₃ at the water interface. HNO₃ exhibits even higher solubility than N_2O_5 . Consequently, despite the presence of NO_2 in the gas, NO_2^- (aq) concentrations in the water remained negligible, while NO_3^- (aq) concentrations significantly increased, confirming the dominant role of N_2O_5 and HNO₃. HNO₃ formation also occurred within the tubing system due to residual water, potentially contributing up to 24% of the measured NO_3^- (aq), even when using dry synthetic air.

The results obtained enhance our understanding of nitrogen fixation processes. Utilizing O_3 can significantly improve $NO_3^-(aq)$ formation efficiency by converting NO and NO_2 to N_2O_5 . Further energy efficiency improvements are possible by optimizing O_3 generation, as in this study a substantial portion of the generated O_3 was not utilized. Future research will focus on optimizing the process by: (1) increasing NO_x generation through tuning the TS discharge driving circuit, (2) improving O_3 generation efficiency, (3) optimizing gas flow



rates, and (4) enhancing the transport of gas-phase products to the aqueous phase. We also plan to investigate this process using humid air treated by TS discharge. This approach may enable direct production of highly soluble HNO₂ via TS discharge and potentially increase HNO₃ formation upon O₃ addition.

Supplementary Information The online version contains supplementary material available at https://doi.org/10.1007/s11090-025-10604-w.

Acknowledgements Funded by the EU NextGenerationEU through the Recovery and Resilience Plan for Slovakia under the project No. 09I03-03-V03-00033; and by the Slovak Research and Development Agency under the Contract No. APVV-20-0566.

Author Contribution P.P. conceptualized the study, developed the methodology, performed formal analysis and investigation, and wrote the original draft. G.S. curated the data, conducted formal analysis, and contributed to reviewing the manuscript. K.H. performed formal analysis and contributed to manuscript review and editing. M.J. provided conceptual guidance, secured funding, supervised the project, and contributed to review and editing. All authors reviewed the manuscript.

Funding Open access funding provided by The Ministry of Education, Science, Research and Sport of the Slovak Republic in cooperation with Centre for Scientific and Technical Information of the Slovak Republic. NextGenerationEU through the Recovery and Resilience Plan for Slovakia under the project No. 09I03-03-V03-00033, Slovak Research and Development Agency APVV-20-0566.

Data Availability Data will be made available by the corresponding authors upon reasonable request.

Open Access This article is licensed under a Creative Commons Attribution 4.0 International License, which permits use, sharing, adaptation, distribution and reproduction in any medium or format, as long as you give appropriate credit to the original author(s) and the source, provide a link to the Creative Commons licence, and indicate if changes were made. The images or other third party material in this article are included in the article's Creative Commons licence, unless indicated otherwise in a credit line to the material. If material is not included in the article's Creative Commons licence and your intended use is not permitted by statutory regulation or exceeds the permitted use, you will need to obtain permission directly from the copyright holder. To view a copy of this licence, visit https://creativecommons.org/licenses/by/4.0/.

References

- Fridman A (2008) Plasma chemistry. Cambridge University Press. https://doi.org/10.1017/CBO978051 1546075
- Kossyi I, Kostinsky AY, Matveyev A, Silakov V (1992) Kinetic scheme of the non-equilibrium discharge in nitrogen-oxygen mixtures. Plasma Sources Sci Technol 1:207. https://doi.org/10.1088/0963-0252/19/4/045025
- Bruggeman P, Schram DC (2010) On OH production in water containing atmospheric pressure plasmas. Plasma Sources Sci Technol. https://doi.org/10.1088/0963-0252/19/4/045025
- Lu X, Naidis GV, Laroussi M, Reuter S, Graves DB, Ostrikov K (2016) Reactive species in non-equilibrium atmospheric-pressure plasmas: generation, transport, and biological effects. Phys Rep 630:1–84. h ttps://doi.org/10.1016/j.physrep.2016.03.003
- Janda M, Hensel K, Tóth P, Hassan ME, Machala Z (2021) The role of HNO2 in the generation of plasma-activated water by air transient spark discharge. Appl Sci 11:7053. https://doi.org/10.3390/app1 1157053
- Trunec D, Navrátil Z, Tomeková J, Mazánková V, Ďurčányová S, Zahoranová A (2022) Chemical composition of gaseous products generated by coplanar barrier discharge in air and N2/O2 mixtures. Plasma Sources Sci Technol 31(11):115011. https://doi.org/10.1088/1361-6595/ac9c8f
- Zhou R, Zhou R, Wang P, Xian Y, Mai-Prochnow A, Lu X, Cullen P, Ostrikov KK, Bazaka K (2020) Plasma-activated water: generation, origin of reactive species and biological applications. J Phys D Appl Phys 53:303001. https://doi.org/10.1088/1361-6463/ab81cf



- Lukes P, Dolezalova E, Sisrova I, Clupek M (2014) Aqueous-phase chemistry and bactericidal effects from an air discharge plasma in contact with water: evidence for the formation of peroxynitrite through a pseudo-second-order post-discharge reaction of H₂O₂ and HNO₂. Plasma Sources Sci Technol 23:015019 https://doi.org/10.1088/0963-0252/23/1/015019
- 9. Wang H, Han R, Yuan M, Li Y, Yu Z, Cullen PJ, Qijing D, Yang Y, Wang J (2023) Evaluation of plasmaactivated water: efficacy, stability, physicochemical properties, and mechanism of inactivation against Escherichia coli. LWT 184:114969. https://doi.org/10.1016/j.lwt.2023.114969
- Machala Z, Tarabová B, Sersenová D, Janda M, Hensel K (2018) Chemical and antibacterial effects of plasma activated water: correlation with gaseous and aqueous reactive oxygen and nitrogen species, plasma sources and air flow conditions. J Phys D Appl Phys 52:034002. https://doi.org/10.1088/1361-6 463/aae807
- Pipliya S, Kumar S, Babar N, Srivastav PP (2023) Recent trends in non-thermal plasma and plasma activated water: effect on quality attributes, mechanism of interaction and potential application in food & agriculture. Food Chemistry Advances. https://doi.org/10.1016/j.focha.2023.100249
- Kooshki S, Pareek P, Mentheour R, Janda M, Machala Z (2023) Efficient treatment of bio-contaminated wastewater using plasma technology for its reuse in sustainable agriculture. Environ Technol Innov 32:103287. https://doi.org/10.1016/j.eti.2023.103287
- Shang K, Li W, Wang X, Lu N, Jiang N, Li J, Wu Y (2019) Degradation of p-nitrophenol by DBD plasma/Fe2+/persulfate oxidation process. Sep Purif Technol 218:106–112. https://doi.org/10.1016/j.seppur.2019.02.046
- Shang K, Morent R, De Geyter N, Wang Y, Yang Z (2025) Plasma catalytic degradation of sulfamethoxazole in water with Fe/Mn-LDO catalyst: performance and mechanism. Sep Purif Technol 360:131145. https://doi.org/10.1016/j.seppur.2024.131145
- Hsieh KC, Wandell RJ, Bresch S, Locke BR (2017) Analysis of hydroxyl radical formation in a gas-liquid electrical discharge plasma reactor utilizing liquid and gaseous radical scavengers. Plasma Process Polym 14:1600171. https://doi.org/10.1002/ppap.201600171
- Gorbanev Y, O'Connell D, Chechik V (2016) Non-thermal plasma in contact with water: the origin of species. Chem Eur J 22:3496–3505. https://doi.org/10.1002/chem.201503771
- Kanazawa S, Kawano H, Watanabe S, Furuki T, Akamine S, Ichiki R, Ohkubo T, Kocik M, Mizeraczyk J (2011) Observation of OH radicals produced by pulsed discharges on the surface of a liquid. Plasma Sources Sci Technol 20(3):034010. https://doi.org/10.1088/0963-0252/20/3/034010
- Pareek P, Kooshki S, Tóth P, Janda M (2024) Tuning composition of plasma activated water generated by transient spark discharge with electrospray. Chem Eng J. https://doi.org/10.1016/j.cej.2024.152583
- Hassan ME, Janda M, Machala Z (2021) Transport of gaseous hydrogen peroxide and ozone into bulk water vs. electrosprayed aerosol. Water 13:182. https://doi.org/10.3390/w13020182
- Hassan ME, Janda M, Machala Z (2025) Comparison of the transport of reactive nitrogen plasma species into water bulk vs. aerosolized microdroplets. Plasma Chem Plasma Process 45:161–189. https://doi.org/10.1007/s11090-024-10511-6
- Lukes P, Locke BR, Brisset J-L (2012) Aqueous-phase chemistry of electrical discharge plasma in water and in gas-liquid environments. Plasma Chem Catalysis in Gases and Liquids 1:243–308. https://doi.or g/10.1002/9783527649525.ch7
- Wang Z, Wang X, Xu S, Zhou R, Zhang M, Li W, Zhang Z, Wang L, Chen J, Zhang J (2024) Off-site
 production of plasma-activated water for efficient disinfection: the crucial role of high valence NOx and
 new chemical pathways. Water Res 267:122541. https://doi.org/10.1016/j.watres.2024.122541
- Luo J, Nie L, Liu D, Lu X (2023) Electrodeless discharge in water: reactive species in liquid and gas phase and energy cost for nitrogen fixation. Plasma Process Polym 20:2200181. https://doi.org/10.1002/ppap.202200181
- Vervloessem E, Aghaei M, Jardali F, Hafezkhiabani N, Bogaerts A (2020) Plasma-based N2 fixation into NO x: insights from modeling toward optimum yields and energy costs in a gliding arc plasmatron. ACS Sustain Chem Eng 8:9711–9720. https://doi.org/10.1021/acssuschemeng.0c01815
- Jõgi I, Erme K, Raud J, Laan M (2016) Oxidation of NO by ozone in the presence of TiO2 catalyst. Fuel 173:45–51. https://doi.org/10.1016/j.fuel.2016.01.039
- Noori H, Raud J, Talviste R, Jõgi I (2021) Water dissolution of nitrogen oxides produced by ozone oxidation of nitric oxide. Ozone Sci Eng 43:284–294. https://doi.org/10.1080/01919512.2020.1839379
- Wang Z, Zhu M, Liu D, Liu L, Wang X, Chen J, Guo L, Liu Y, Hou M, Rong M (2023) N2O5 in air discharge plasma: energy-efficient production, maintenance factors and sterilization effects. J Phys D Appl Phys 56:075204. https://doi.org/10.1088/1361-6463/acb65f
- Kaneko T, Sasaki S, Takashima K, Higashitani A, Ando S, Takahashi H (2022) (Invited) synthesis of dinitrogen pentoxide using air atmospheric pressure plasmas and application for biomaterial processes. ECS Meet Abstr MA2022-02:894. https://doi.org/10.1149/MA2022-0219894mtgabs



- Gordon IE, Rothman LS, Hargreaves ER, Hashemi R, Karlovets EV, Skinner F, Conway EK, Hill C, Kochanov RV, Tan Y (2022) The HITRAN2020 molecular spectroscopic database. J Quant Spectrosc Radiative Transfer 277:107949. https://doi.org/10.1016/j.jqsrt.2021.107949
- Kochanov RV, Gordon IE, Rothman LS, Shine K, Sharpe SW, Johnson TJ, Wallington T, Harrison JJ, Bernath PF, Birk M (2019) Infrared absorption cross-sections in HITRAN2016 and beyond: expansion for climate, environment, and atmospheric applications. J Quant Spectrosc Radiative Transfer 238:106708. https://doi.org/10.1016/j.jqsrt.2019.04.001
- 31. Liu Z, Zhou C, Liu D, He T, Guo L, Xu D, Kong MG (2019) Quantifying the concentration and penetration depth of long-lived RONS in plasma-activated water by UV absorption spectroscopy. AIP Adv. https://doi.org/10.1063/1.5037660
- Oh J-S, Szili EJ, Ogawa K, Short RD, Ito M, Furuta H, Hatta A (2017) UV–vis spectroscopy study of plasma-activated water: dependence of the chemical composition on plasma exposure time and treatment distance. Jpn J Appl Phys 57:0102B9. https://doi.org/10.7567/JJAP.57.0102B9
- Brown CW, Lynch PF, Obremski RJ, Lavery DS (1982) Matrix representations and criteria for selecting analytical wavelengths for multicomponent spectroscopic analysis. Anal Chem 54:1472–1479. https:// doi.org/10.1021/ac00246a007
- He B, Ma Y, Gong X, Long Z, Li J, Xiong Q, Liu H, Chen Q, Zhang X, Yang S (2017) Simultaneous quantification of aqueous peroxide, nitrate, and nitrite during the plasma—liquid interactions by derivative absorption spectrophotometry. J Phys D Appl Phys 50:445207. https://doi.org/10.1088/1361-6463/ aa8819
- Van Gaens W, Bogaerts A (2014) Reaction pathways of biomedically active species in an Ar plasma jet. Plasma Sources Sci Technol 23:035015. https://doi.org/10.1088/0963-0252/23/3/035015
- S. Pancheshnyi, B. Eismann, G. Hagelaar, L. Pitchford, Computer Code ZDPlasKin (Toulouse: University of Toulouse) LAPLACE, CNRS-UPS-INP (www. zdplaskin. laplace. univ-tlse. fr), 2008.
- Brown PN, Byrne GD, Hindmarsh AC (1989) VODE: a variable-coefficient ODE solver. SIAM J Sci Stat Comput 10(5):1038–1051. https://doi.org/10.1137/0910062
- kinet_N2_O2_v1.03, 2015, (n.d.). http://www.zdplaskin.laplace.univ-tlse.fr/wp-content/uploads/2015/ 08/kinet_N2_O2_v1.03.inp.
- Capitelli M, Ferreira CM, Gordiets BF, Osipov AI (2013) Plasma kinetics in atmospheric gases. Springer Science & Business Media. https://doi.org/10.1007/978-3-662-04158-1
- Flitti A, Pancheshnyi S (2009) Gas heating in fast pulsed discharges in N2–O2 mixtures. Eur Phys J Appl Phys 45:21001. https://doi.org/10.1051/epjap/2009011
- Hagelaar G, Pitchford LC (2005) Solving the Boltzmann equation to obtain electron transport coefficients and rate coefficients for fluid models. Plasma Sources Sci Technol 14:722. https://doi.org/10.10 88/0963-0252/14/4/011
- Janda M, Martišovitš V, Machala Z (2011) Transient spark: a dc-driven repetitively pulsed discharge and its control by electric circuit parameters. Plasma Sources Sci Technol 20(3):035015. https://doi.org/10.1088/0963-0252/20/3/035015
- Janda M, Machala Z, Niklová A, Martišovitš V (2012) The streamer-to-spark transition in a transient spark: a dc-driven nanosecond-pulsed discharge in atmospheric air. Plasma Sources Sci Technol 21:045006. https://doi.org/10.1088/0963-0252/21/4/045006
- Janda M, Hensel K, Machala Z, Field TA (2023) The influence of electric circuit parameters on NOx generation by transient spark discharge. J Phys D Appl Phys 56:485202 https://doi.org/10.1088/1361-6 463/ace634
- Komiyama H, Inoue H (1980) 20 absorption of nitrogen oxides into water. Chem Eng Sci 35:154–161. https://doi.org/10.1016/0009-2509(80)80082-0
- Sander R (2015) Compilation of Henry's law constants (version 4.0) for water as solvent. Atmos Chem Phys 15:4399–4981. https://doi.org/10.5194/acp-15-4399-2015
- Wagner I, Strehlow H (1982) Flash photolysis in aqueous periodate-solutions. Ber Bunsenges Phys Chem 86:297–301. https://doi.org/10.1002/bbpc.19820860408
- Treinin A, Hayon E (1970) Absorption spectra and reaction kinetics of NO2, N2O3, and N2O4 in aqueous solution. J Am Chem Soc 92:5821–5828. https://doi.org/10.1021/ja00723a001
- Wayne RP, Barnes I, Biggs P, Burrows J, Canosa-Mas C, Hjorth J, Le Bras G, Moortgat G, Perner D, Poulet G (1991) The nitrate radical: physics, chemistry, and the atmosphere. Atmospheric Environment. Part A. General Topics 25:1–203. https://doi.org/10.1016/0960-1686(91)90192-A
- Wahner A, Mentel TF, Sohn M (1998) Gas-phase reaction of N2O5 with water vapor: importance of heterogeneous hydrolysis of N2O5 and surface desorption of HNO3 in a large Teflon chamber. Geophys Res Lett 25:2169–2172. https://doi.org/10.1029/98GL51596
- Mentel TF, Bleilebens D, Wahner A (1996) A study of nighttime nitrogen oxide oxidation in a large reaction chamber—the fate of NO2, N2O5, HNO3, and O3 at different humidities. Atmos Environ 30:4007–4020. https://doi.org/10.1016/1352-2310(96)00117-3



52. Chang WL, Bhave PV, Brown SS, Riemer N, Stutz J, Dabdub D (2011) Heterogeneous atmospheric chemistry, ambient measurements, and model calculations of N2O5: a review. Aerosol Sci Technol 45:665–695. https://doi.org/10.1080/02786826.2010.551672

Publisher's Note Springer Nature remains neutral with regard to jurisdictional claims in published maps and institutional affiliations.

